Physics – Uspekhi **62** (11) 1136 – 1152 (2019)

CONFERENCES AND SYMPOSIA

PACS numbers: 04.30.Tv, 97.10.Gz, **97.80. – d**

Possible electromagnetic manifestations of merging black holes

D V Bisikalo, A G Zhilkin, E P Kurbatov

DOI: https://doi.org/10.3367/UFNe.2019.04.038591

Contents

Abstract. The accretion disk response to a loss of 5% of the mass of the accretor formed by a stellar-mass binary black hole coalescence has been simulated. The parameters of the initial binary system correspond to the gravitational-wave source GW170814. We performed a series of simulations of models with radiative and convective heat transfer mechanisms and various accretion rates. The models took into account radiation pressure and adiabatic vertical gas expansion. Reducing the mass of the accretor due to emission of gravitational waves led to a strong hydrodynamic disturbance of the disk that developed in less than one second into a shock wave. As a result of shock heating, the luminosity of convective disks increased by 3–5 orders of magnitude and reached 10^{43} erg s^{-1}. The luminosity of radiative disks increased by 1–2 orders of magnitude, to 10^{40} erg s^{-1}. If the source is as far as 540 Mpc (as in the case of the GW170814 event), disk brightening could be detected by the XMM-Newton X-ray observatory.

Keywords: gravitational waves, black holes, binary stars, black hole merging, accretion disks

1. Introduction

A system of two orbiting gravitating bodies is known to emit gravitational waves (GWs) [1]. The waves take away energy and, due to the anisotropy of radiation, momentum. As a result, the components of the binary system come closer to each other and merge. According to theoretical concepts, binary black holes (BHs) exhibit the highest intensity of GW radiation [2], and binary BHs of stellar masses have the highest probability of detection [3, 4]. Beginning in 2015, several GW events accompanying the merger of BH pairs were detected by the LIGO (Laser Interferometer Gravitational-wave Observatory) and Virgo detectors (see [5] and references therein). The pairs were located at distances ranging from several hundred to several thousand Mpc, which corresponds to a merger frequency [1] of the order of 100 Gpc^{-3} yr^{-1}.

A consequence of the energy loss by a binary system in emitting gravitational waves is that the merger product mass is several percent less than the mass of the original binary system [8]. Due to the loss of momentum, the object receives a kick [9], gaining as a result a speed of up to 1000 km s^{-1} [10].

If the binary system is surrounded by a shell or an accretion disk, then the substance of the disk is disturbed as a result of merging. Possible destabilization of the accretion disk due to the loss of mass of a binary BH was hypothesized for the first time in [11]. It was shown in [12] that the BH recoil effect and subsequent gravitational perturbation can excite shock waves in the disk. Finally, perturbations of the metric themselves cause mechanical stresses in the disk that can dissipate on a viscous time scale [13] or transform into shock waves [14]. These phenomena should lead to a response from the accretion disk in the form of electromagnetic radiation: an increase in luminosity and quasiperiodic bursts.

Previously, a number of studies on this topic explored the merging of supermassive BHs in nuclei of galaxies (see, for example, [12, 15–17]). Thus, if a binary BH with a total mass of $10^6\,M_\odot$ loses 5% of its mass after merging, then the luminosity of the accretion disk increases by an order of magnitude, to 10^{43} erg s^{-1} [16]. The effect of the recoil momentum leads to a comparable increase in luminosity; however, its magnitude substantially depends on poorly determined parameters of the merging binary system [18,

[1] Population synthesis models predict a higher rate of mergers [3, 6, 7].

D V Bisikalo (*), **A G Zhilkin** (†), **E P Kurbatov** (‡)
Institute of Astronomy, Russian Academy of Sciences,
ul. Pyatnitskaya 48, 119017 Moscow, Russian Federation
E-mail: (*) bisikalo@inasan.ru, (†) zhilkin@inasan.ru,
(‡) kurbatov@inasan.ru

Received 13 June 2019
Uspekhi Fizicheskikh Nauk **189** (11) 1213 – 1229 (2019)
DOI: https://doi.org/10.3367/UFNr.2019.04.038591
Translated by M Zh Shmatikov; edited by V L Derbov

19]. With regard to stellar-mass BHs, estimates of accretion disk brightening to $10^{42}-10^{43}$ erg s^{-1} were also obtained, with a maximum located in the X-ray part of the spectrum [20].

The scenario of disk formation around a supermassive BH is quite obvious: the merging of galaxies, in which the merger product preserves an angular momentum large enough to maintain disk morphology. In a stellar-mass BH, there are several ways of forming a circumbinary disk: the disk matter can originate from a molecular cloud, wind from a third star in the hierarchical system, the remains of a star destroyed by tidal effects, etc. It was suggested in [21] that a binary BH emerges due to rotational instability during the collapse of the core of a massive star ($> 100\,M_\odot$), while the shell of the star becomes an electromagnetic radiation source.

We present here the development of our studies on the response of a circumbinary accretion disk in a binary stellar BH system to a loss of 5% of the accretor mass [22]. In addition to calculating the accretion disk with gas pressure dominance [22], we have developed a numerical model and performed two series of calculations of how perturbations develop: in the accretion disk with consideration of radiation pressure and the adiabatic heating and cooling of the disk due to the vertical motion of matter. The binary system parameters correspond to event GW170814, namely, the merger of a binary BH with component masses of $30.5^{+5.7}_{-3.0}\,M_\odot$ and $25.3^{+2.8}_{-4.2}\,M_\odot$ [23]. We have analyzed the applicability of the models and calculated light curves and electromagnetic radiation spectra at maximum brightness. The bulk of the electromagnetic radiation energy proved to be emitted in the X-ray range and attains 10^{43} erg s^{-1}. A burst that may continue for up to several hundred seconds is detectable using currently available instruments.

The paper is organized as follows. Section 2 briefly describes the structure of an accretion disk with radiative and convective heat transport mechanisms and presents a formulation of the problem. Sections 3–5 contain a description of models and calculations for disks with gas pressures that take into account radiation pressure and vertical expansion/contraction. Section 6 presents the results obtained.

2. Formulation of the problem

At the time when study [5] was under preparation, the LIGO and Virgo observatories published a description of 10 events of binary BH mergers that they discovered, of which only five had no artifacts. These events are presented in Table 1 together with estimates of the masses of the components and the proportion of the mass lost.

The lifetime of a binary BH prior to a merger can be estimated as the characteristic time of loss of angular momentum by a close binary system with circular orbits [7]:

$$\tau_{\rm GWR} = (10^8 \text{ years})\left(\frac{a}{R_\odot}\right)^4 \frac{M_\odot^3}{M_1 M_2\,(M_1+M_2)}\,, \qquad (1)$$

where a is the distance between the components and M_1 and M_2 are the masses of the components. For example, for a binary BH with masses of the components of $30\,M_\odot$ and $25\,M_\odot$ to merge in the Hubble time, 13.7×10^9 years, the initial distance between its components may not exceed $48\,R_\odot$.

The radius of the inner boundary of the disk is determined by the balance between the tidal force from the binary BH and the force of viscous (turbulent) friction in the disk matter [24]. This quantity can be estimated from below as the radius at which tidal and gravitational accelerations from a pointlike accretor of the same mass are equal:

$$\frac{2GM}{r_{\rm in}^2}\,\frac{a/2}{r_{\rm in}} = \frac{GM}{r_{\rm in}^2}\,. \qquad (2)$$

We have then $r_{\rm in} > a$. Actually, gas-dynamic effects result in an increase in the inner radius of the disk, which is confirmed by the results of numerical calculations. For example, it was shown in [24] that the inner boundary of the circumbinary disc becomes established, for a zero-eccentricity binary system, at a radius of $1.8\,a$. The binary BH begins merging if $a \approx 6\,r_{\rm g}$, where $r_{\rm g} = 2GM/c^2 = (4.2\times10^{-6}\,R_\odot)\,m$ is the gravitational radius of the accretor. Up to this moment, the components approach each other slowly and, owing to the viscous force, the disk has enough time to adjust to the changing distance between the components. Of interest for us is the state of the accretion disk immediately at the moment of merging; therefore, we assume below that $r_{\rm in} \equiv 10\,r_{\rm g}$, a value that is consistent with the results of [24–26].

We take as a basis the standard α-model of Shakura and Sunyaev for a geometrically thin Keplerian disk [27]. The accretion rate is determined in this model by the rate of dissipation of the angular momentum for which turbulent viscosity is responsible. The turbulence intensity is characterized by a parameter α that usually does not exceed one. The rate of dissipation of the kinetic energy of the rotational motion of the disk matter also determines the rate of energy release in the disk and affects its thermal structure, i.e., the distribution of density and temperature.

The disk structure in the α-model depends on the dimensionless accretor mass $m \equiv M/M_\odot$, the dimensionless accretion rate $\dot m \equiv \dot M/\dot M_{\rm cr}$, the turbulence parameter α, and the inner radius of the disk $r_{\rm in}$. The critical accretion rate $\dot M_{\rm cr}$ is determined by the Eddington luminosity:

$$\dot M_{\rm cr} = \left(3\times10^{-8}\,\frac{M_\odot}{\rm year}\right)\frac{0.06}{\eta}\,m\,, \qquad (3)$$

Table 1. Parameters of binary merging BHs according to gravitational-wave observations. Columns, from left to right: name of the object, mass of components, relative change in mass, distance to the object.

Object	$M_1/M_\odot$, $M_2/M_\odot$	$\Delta M/(M_1+M_2)$, %	D, Mpc	References
GW150914	36^{+5}_{-4}, 29^{+4}_{-4}	3.3 – 5.2	410^{+160}_{-180}	[47]
GW151226	$14.2^{+8.3}_{-3.7}$, $7.5^{+2.3}_{-2.3}$	2.9 – 5.5	440^{+180}_{-190}	[48]
GW170104	$31.2^{+8.4}_{-6.0}$, $19.4^{+8.3}_{-5.9}$	2.3 – 5.7	880^{+450}_{-390}	[49]
GW170608	12^{+7}_{-2}, 7^{+2}_{-2}	2.8 – 5.1	340^{+140}_{-140}	[50]
GW170814	$30.5^{+5.7}_{-3.0}$, $25.3^{+2.8}_{-4.2}$	4.0 – 5.8	540^{+130}_{-210}	[23]

where η is the efficiency of the emission of gravitational energy (accretion efficiency). In the case of a single nonrotating BH, $\eta = 0.06-0.08$ [28]. If rotation is taken into account, the stationary accretion efficiency increases to ~ 0.32 [29, 30]. In the scenario of episodic accretion, η may be as large as 0.43 [31]. Some authors have suggested that the tidal effect of the binary system slows down the accretion (see, for example, [32]). However, the value of the accretion efficiency parameter in the model under consideration is not critical, since a decisive role is played by the dimensionless accretion rate $\dot{m}$. We set $\eta = 0.06$.

We also assume for rough estimates that $m \lesssim 10^2$, $\dot{m} \lesssim 1$, and $\alpha \sim 0.01$; then, the characteristic density in the inner region of the disk, in its middle plane, is $\rho \sim 1$ g cm^{-3}, temperature $T \sim 10^7$ K, and semi-thickness $H \sim 0.01\, r_{\rm in}$ [22]. With these parameters, the optical semi-thickness of the disk is $\tau_{\rm R} \sim [\kappa_{\rm R}^{\rm ff} + \kappa^{\rm es}]\Sigma/2 \gtrsim 10^5$, where $\kappa_{\rm R}^{\rm ff} = 0.11 N/T^{7/2}$ cm^2 g^{-1} is the Rosseland opacity coefficient determined by free-free (ff) transitions, $\kappa^{\rm es} = 0.40$ cm^2 g^{-1} is the opacity coefficient determined by electron-electron (ee) scattering, and $\Sigma \sim 2H\rho$ is the surface density. The main contribution to opacity in the outer parts of the disk comes from free-free transitions; the optical thickness there is also about 10^4-10^5. Since $\tau_{\rm R} \gg 1$, the radiation flux $F_{\rm s}$ per unit disk surface and surface temperature $T_{\rm s}$ are related by the formula

$$\sigma_{\rm SB} T_{\rm s}^4 \approx F_{\rm s}\,, \tag{4}$$

where $\sigma_{\rm SB} = 5.67 \times 10^{-5}$ erg cm^{-2} s^{-1} K^{-4}. At the same time, the rate of energy release per unit disk area in the vicinity of the inner boundary will be [27]

$$Q \approx \frac{3\dot{M}}{8\pi}\,\Omega^2\bigg|_{r_{\rm in}} = \left(10^{24}\ {\rm erg\ cm^{-2}\ s^{-1}}\right)\frac{\dot{m}}{m}\,, \tag{5}$$

where $\Omega = (GM/r^3)^{1/2}$ is the Keplerian velocity distribution. If we define the radiation flux as the rate of energy release on one side of the disk, then $F_{\rm s} = Q/2$.

Let us assume that thermal energy is transported in a radiative way. Then, based on fairly general considerations, it can be argued that the radiation flux density and gas temperature at the center of the disk $T_{\rm c}$ are related as [33]

$$\sigma_{\rm SB} T_{\rm c}^4 = \left(\frac{3\tau_{\rm R}}{8} + \frac{1}{2} + \frac{1}{4\tau_{\rm P}}\right)F_{\rm s}\,, \tag{6}$$

where $\tau_{\rm P} \sim \kappa_{\rm P}\Sigma/2$ is the half thickness of the disk determined by the Planck opacity coefficient $\kappa_{\rm P}^{\rm ff} = 4.13 N/T^{7/2}$ cm^2 g^{-1}. With the accepted parameters of the disk $\tau_{\rm P} \gg 1$, therefore,

$$\sigma_{\rm SB} T_{\rm c}^4 \approx \frac{3\tau_{\rm R}}{8}\,F_{\rm s}\,. \tag{7}$$

With consideration for Eqn (4), we obtain

$$\frac{T_{\rm c}}{T_{\rm s}} \approx \left(\frac{3\tau_{\rm R}}{8}\right)^{1/4}. \tag{8}$$

Given the estimates of the optical thickness made above, we find $T_{\rm c} \approx 14\, T_{\rm s}$.

It was shown in [34] that an optically thick α-disk whose structure is determined by the pressure of an ideal gas is convectively stable. This is true at least when disk opacity is determined by free-free transitions or Thomson scattering; moreover, it holds valid regardless of the accretion rate and accretor mass. On the other hand, the possibility that convection develops even in disks that are obviously stable according to the local Schwarzschild criterion [35] is not ruled out. In addition, depending on the specific type of turbulent viscosity coefficient as a function of gas parameters, thermal instability may develop in the disk [32, 36]. This issue is also complicated by the possible presence of a magnetic field whose role is unclear. On the one hand, for α-disks, the ratio of turbulent pressure to the gas pressure is of the order of $\alpha^2 \ll 1$, so even a weak magnetic field should affect convection up to its complete suppression with field enhancement. On the other hand, magnetorotational instability is possible [37] in disks with a weak magnetic field, which leads to disk turbulization [38, 39].

If we assume that there is a developed convection in the disk, the temperature difference between the middle layer and the surface can be estimated as the difference between the corresponding temperatures for the isentropic vertical structure of the disk. The temperature changes on the height scale of the radiative disk by more than an order of magnitude, and the density changes by about a factor of two [27]; hence, the temperature ratio $T_{\rm c}/T_{\rm s}$ would be $2^{\gamma-1} \approx 1.6$, where $\gamma = 5/3$ is the adiabatic exponent for a monatomic gas. To take into account the possibility of both radiative heat transport and developed convection, we perform calculations for two series of models, where the means of heat transport are parameterized by

$$f_{\rm ht} = \frac{T_{\rm c}}{T_{\rm s}}\,. \tag{9}$$

We set for convective disks $f_{\rm ht} \equiv 2$, while for radiative disks, $f_{\rm ht} \equiv 10$.

In the radiative α-disk model, three characteristic zones can be distinguished in the general case, in which the distribution of hydrodynamic quantities depends on whether gas or radiation pressure prevails and what process determines opacity. The vertical structure of the disc in these zones is rather different a lot. However, the radial dependences of the density and temperature are close to power laws with approximately the same exponents. Therefore, we assume in all numerical calculations that the temperature and density in the middle of the equilibrium disk are distributed according to a power law,

$$T_{\rm c} = T_*\left(\frac{r}{r_*}\right)^{-k_{\rm t}}, \qquad k_{\rm t} = \frac{9}{10}\,, \tag{10}$$

$$\rho_{\rm c} = \rho_*\left(\frac{r}{r_*}\right)^{-k_{\rm d}}, \qquad k_{\rm d} = \frac{33}{20}\,. \tag{11}$$

Dependences (10) and (11) correspond to the so-called zone B in the α-disk model. The main contribution to the thermodynamic pressure in zone B comes from gas pressure, while the role of radiation pressure is rather insignificant. The gas temperature is in this case high enough for the opacity of the medium to be determined by Thomson scattering alone. We set the characteristic scale r_* equal to the inner radius of the disk $r_{\rm in} = 10\, r_{\rm g} = (4.2 \times 10^{-5}\, R_\odot)\, m$. The temperature scale is normalized to the rate of energy release at the inner radius of the disk, according to Eqns (4) and (5):

$$T_* = f_{\rm ht}\, T_{\rm s}\Big|_{r_{\rm in}} = (10^7\ {\rm K})\, f_{\rm ht}\left(\frac{\dot{m}}{m}\right)^{1/4}. \tag{12}$$

The density at the inner boundary of the disk corresponds to zone B [22]:

$$\rho_* = (0.76\ \mathrm{g\ cm^{-3}})\,(\alpha m)^{-7/10}\dot{m}^{2/5}\,. \tag{13}$$

The distribution of angular momentum over the disk is close to Keplerian, and the relative contribution of pressure to the radial balance of forces is of the order of $(H_*/r_{\rm in})^2 \sim 10^{-4}$. Based on this, we disregard the radial velocity of the gas in the initial configuration of the disk.

We are now in position to formulate the problem. There is a stationary accretion disk in a gravitational field of a pointlike mass. The disk features a power-law distribution of temperature and density along the radius. The centrifugal force balances the force of gravity and gas pressure, the radial velocity of the gas being everywhere equal to zero. The accretor loses at the initial moment 5% of its mass. As a result, the balance of radial forces is disturbed. Further evolution of the disk is calculated in the approximation of nondissipative gas dynamics. Of interest to us is the solution in the middle plane of the disk. Vertical gas motion is accounted for in Section 5.

3. Disk with gas pressure

The equations of the nondissipative radial axisymmetric flow in the Eulerian formulation have the form

$$\frac{\partial\rho}{\partial t} + \frac{1}{r}\frac{\partial(r\rho v)}{\partial r} = 0\,, \tag{14}$$

$$\frac{\partial v}{\partial t} + v\frac{\partial v}{\partial r} + \frac{1}{\rho}\frac{\partial P}{\partial r} - \frac{L^2}{r^3} + (1-\xi)\frac{GM}{r^2} = 0\,, \tag{15}$$

$$\frac{\partial L}{\partial t} + v\frac{\partial L}{\partial r} = 0\,, \tag{16}$$

$$\frac{\partial E}{\partial t} + v\frac{\partial E}{\partial r} + \frac{P}{\rho}\frac{1}{r}\frac{\partial(rv)}{\partial r} = 0\,. \tag{17}$$

Here, L is the angular momentum per unit mass. The equation for the radial projection of velocity contains the parameter ξ — the fraction of the initial rest mass M of the accretor lost on the radiation of gravitational waves.

We only consider the contribution of gas to pressure. Then,

$$P = A\rho T\,, \qquad E = \frac{AT}{\gamma-1}\,. \tag{18}$$

At the initial moment, the configuration is in equilibrium ($\xi = 0$), the radial velocity is zero, and the temperature and density distributions are described by power laws (10) and (11). From the condition of radial equilibrium at the initial moment,

$$\frac{1}{\rho}\frac{\partial P_0}{\partial r} - \frac{L_0^2}{r^3} + \frac{GM}{r^2} = 0\,, \tag{19}$$

we obtain

$$L_0 = r_* c_* \left[\mu^2 - (k_{\rm d}+k_{\rm t})\left(\frac{r}{r_*}\right)^{1-k_{\rm t}}\right]^{1/2}\left(\frac{r}{r_*}\right)^{1/2}, \tag{20}$$

where $c_*^2 = AT_*$,

$$\mu = \left(\frac{GM}{r_* c_*^2}\right)^{1/2}. \tag{21}$$

In its meaning, the parameter μ is equal to the Mach number at the radius r_*.

For subsequent estimates, we need an expression for the half thickness of the disk. We define it as a vertical scale of the equilibrium disk

$$H = \frac{(AT)^{1/2}}{L/r^2} = r_*\left[\mu^2\left(\frac{r}{r_*}\right)^{k_{\rm t}-1} - (k_{\rm d}+k_{\rm t})\right]^{-1/2}\frac{r}{r_*}\,. \tag{22}$$

3.1 Self-similar waves

The system of equations (14)–(17) allows a self-similar solution if the exponents in (10) and (11) in the equilibrium disk are set equal to $k_{\rm d} = 3/2$ and $k_{\rm t} = 1$. The initial distributions then take the form

$$\rho_0 = \rho_*\left(\frac{r}{r_*}\right)^{-3/2}, \tag{23}$$

$$E_0 = \frac{c_*^2}{\gamma-1}\left(\frac{r}{r_*}\right)^{-1}, \tag{24}$$

$$L_0 = r_* c_*\left(\mu^2 - \frac{5}{2}\right)^{1/2}\left(\frac{r}{r_*}\right)^{1/2}. \tag{25}$$

We define hydrodynamic quantities in the following way:

$$\rho(t,r) = \rho_0(r)\sigma(\lambda)\,, \tag{26}$$

$$E(t,r) = E_0(r)a(\lambda)\,, \tag{27}$$

$$v(t,r) = \frac{r}{t}\,u(\lambda)\,, \tag{28}$$

$$L(t,r) = L_0(r)\Lambda(\lambda)\,, \tag{29}$$

where σ, a, u, and Λ are self-similar density, energy, speed, and specific angular momentum, respectively. Their dependence on the radial coordinate and time reduces to the dependence on the parameter

$$\lambda = \frac{r/r_*}{(t/t_*)^{2/3}}\,, \tag{30}$$

where $t_* = r_*/c_*$. Thus, there is a nondegenerate self-similarity of the first type [40].

After substituting formulas (26)–(30), the system of equations (14)–(17) is reduced to the dimensionless form

$$\left(u - \frac{2}{3}\right)\frac{\mathrm{d}\ln\sigma}{\mathrm{d}\ln\lambda} + \frac{\mathrm{d}u}{\mathrm{d}\ln\lambda} + \frac{u}{2} = 0\,, \tag{31}$$

$$\left(u - \frac{2}{3}\right)\frac{\mathrm{d}u}{\mathrm{d}\ln\lambda} + u(u-1) + \left(\frac{\mathrm{d}\ln(\sigma a)}{\mathrm{d}\ln\lambda} - \frac{5}{2}\right)\frac{a}{\lambda^3} - \left(\mu^2 - \frac{5}{2}\right)\frac{\Lambda^2}{\lambda^3} + \frac{(1-\xi)\,\mu^2}{\lambda^3} = 0\,, \tag{32}$$

$$\left(u - \frac{2}{3}\right)\frac{\mathrm{d}\ln\Lambda}{\mathrm{d}\ln\lambda} + \frac{u}{2} = 0\,, \tag{33}$$

$$\left(u - \frac{2}{3}\right)\frac{3}{2}\frac{\mathrm{d}\ln a}{\mathrm{d}\ln\lambda} + \frac{\mathrm{d}u}{\mathrm{d}\ln\lambda} + \frac{u}{2} = 0\,. \tag{34}$$

Self-similarity parameter (30) tends to infinity at $t \to 0$. This means that, in order to correspond to the initial conditions (23)–(25), the following limits must be valid:

$$\sigma \to 1\,, \quad a \to 1\,, \quad \Lambda \to 1\,, \quad u \to 0 \quad \text{if} \quad \lambda \to \infty\,. \tag{35}$$

It should be noted that, in the absence of a gravitational perturbation ($\xi = 0$), these limits are valid for all λ identically.

Combining first (31) and (33), and then (31) and (34), we can obtain two algebraic integrals:

$$\left(u - \frac{2}{3}\right)\frac{\sigma}{\Lambda} = C_1 \equiv \text{const}\,, \tag{36}$$

$$\left(u - \frac{2}{3}\right)\frac{\mathrm{d}\ln(\sigma/a^{3/2})}{\mathrm{d}\ln\lambda} = 0\,. \tag{37}$$

If $u - 2/3 \neq 0$, then integral (37) takes the form

$$\frac{a}{\sigma^{2/3}} = C_2 \equiv \text{const}\,. \tag{38}$$

The algebraic integrals may be used to reduce system (31)–(34) to two equations. First, we transform (32), excluding the angular momentum and energy:

$$\left(u - \frac{2}{3}\right)\frac{\mathrm{d}u}{\mathrm{d}\ln\lambda} + u(u-1) + \left(\frac{5}{3}\frac{\mathrm{d}\ln\sigma}{\mathrm{d}\ln\lambda} - \frac{5}{2}\right)\frac{C_2\sigma^{2/3}}{\lambda^3} - \left(\mu^2 - \frac{5}{2}\right)\left(u - \frac{2}{3}\right)^2\frac{\sigma^2}{C_1^2\lambda^3} + \frac{(1-\xi)\,\mu^2}{\lambda^3} = 0\,. \tag{39}$$

We then use Eqn (31) to eliminate the velocity derivative and finally to obtain the equation

$$\left[\frac{5}{3}\frac{C_2\sigma^{2/3}}{\lambda^3} - \left(u - \frac{2}{3}\right)^2\right]\frac{\mathrm{d}\ln\sigma}{\mathrm{d}\ln\lambda} = -\left(u - \frac{4}{3}\right)u + \frac{5}{2}\frac{C_2\sigma^{2/3}}{\lambda^3} + \left(\mu^2 - \frac{5}{2}\right)\left(u - \frac{2}{3}\right)^2\frac{\sigma^2}{C_1^2\lambda^3} - \frac{(1-\xi)\,\mu^2}{\lambda^3}\,, \tag{40}$$

which should be solved together with Eqn (31) with the initial conditions (35).

The system of equations (31) and (40) has at least two singular points:

$$u = \frac{2}{3}\,, \tag{41}$$

$$\frac{5}{3}\frac{C_2\sigma^{2/3}}{\lambda^3} = \left(u - \frac{2}{3}\right)^2\,. \tag{42}$$

We will see below that the first one is associated with shock waves. The second singular point is related to the existence of 'caustic' finite singularities. The solution is continuous on caustics, but the derivatives of dimensionless density, internal energy, and velocity experience infinite discontinuity. It can be shown that the dimensionless density in the vicinity of caustic λ_c behaves as $\sigma - \sigma_c \propto -|\lambda - \lambda_c|^{\delta}$, where $0 < \delta < 1$, $0 < \sigma_c < \infty$.

We present for reference a formula for the adiabatic speed of sound squared:

$$c_s^2 = \left(\frac{\partial P}{\partial\rho}\right)_s = c_*^2\left(\frac{r}{r_*}\right)^{-1}\frac{5}{3}\,a\,. \tag{43}$$

The sonic point is determined by the condition $v^2 = c_s^2$ or, in self-similar quantities,

$$u^2 = \frac{5}{3}\frac{a}{\lambda^3}\,. \tag{44}$$

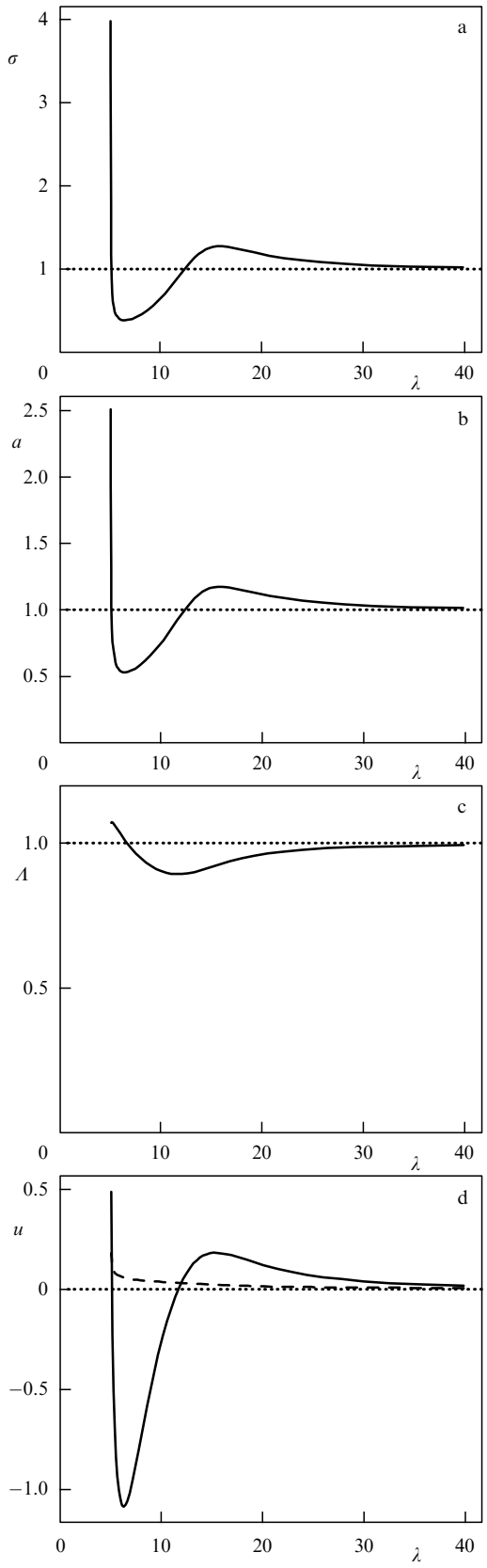

Figure 1. Solution of self-similar equations (31) and (40) for $\mu = 100$, $\xi = 0.05$. The dotted lines correspond to the solution for an unperturbed disk. The dashed curve in Fig. d shows the profile of the dimensionless speed of sound.

Figure 1 shows an example of a numerical solution of system (31) and (40) for $\mu = 100$ and $\xi = 0.05$. The initial

conditions (35) are set at $\lambda = 500$. The caustic is located at approximately $\lambda = 5$. The maximum values of the dimensionless functions increase with increasing parameters μ and ξ.

The solution of the self-similar system beyond the caustic could not be obtained. It should be noted that self-similar equations (31)–(34) describe a continuous gas flow. However, it is clear from general considerations that the internal regions of the disk are more sensitive to perturbations than are its external parts, since the imbalance of gravitational and centrifugal forces increases with decreasing distance to the accretor. As a result of this imbalance, an excess of kinetic energy of the gas emerges that is not compensated by gravitational energy. In this case, the ratio of excess kinetic energy to the thermal energy of the gas is of the order of $\xi\mu^2 \gg 1$. This suggests that the solution must be sought taking into account shock waves.

We show briefly that, if the flow is described by Eqns (14)–(17) and has the initial configuration (23)–(25), then the shock waves in such a flow will be self-similar. Suppose that the shock wave (SW) trajectory $r_D(t)$ corresponds to the self-similar parameter $\lambda = \lambda_D \equiv (r_D/r_*)/(t/t_*)^{2/3}$; the SW velocity is then

$$D = \frac{\mathrm{d}r_D}{\mathrm{d}t} = \frac{2}{3}\,\frac{r_D}{t}\,. \tag{45}$$

Comparing with definition (28), we find that all the SWs have the same self-similar speed, equal to 2/3.

We denote by subscripts 1 and 2 the values of the quantities in front of the SW (from the outer part of the disk) and behind it, respectively. The jump of gas-dynamic quantities is denoted as $[[f]] = f_1 - f_2$. The relation between quantities on opposite sides of the discontinuity is described by the Hugoniot conditions:

$$D[\![\rho]\!] = [\![\rho v]\!]\,, \tag{46}$$

$$D[\![\rho v]\!] = [\![\rho v^2 + (\gamma - 1)\,\rho E]\!]\,, \tag{47}$$

$$D[\![\rho L]\!] = [\![\rho v L]\!]\,, \tag{48}$$

$$D\left[\!\!\left[\rho\left(\frac{v^2}{2} + \frac{L^2}{2r^2} + E\right)\right]\!\!\right] = \left[\!\!\left[\rho v\left(\frac{v^2}{2} + \frac{L^2}{2r^2} + \gamma E\right)\right]\!\!\right]. \tag{49}$$

Similar to Eqns (26)–(29), we define dimensionless quantities:

$$\begin{aligned} &\rho_{1,2} = \rho_0(r_D)\,\sigma_{1,2}\,, \quad E_{1,2} = E_0(r_D)\,a_{1,2}\,,\\ &v_{1,2} = \frac{r_D}{t}\,u_{1,2}\,, \quad L_{1,2} = L_0(r_D)\,\Lambda_{1,2}\,. \end{aligned} \tag{50}$$

Re-written in self-similar variables, the Hugoniot conditions take the form (we took into account that $\gamma = 5/3$)

$$\left[\!\!\left[\left(u - \frac{2}{3}\right)\sigma\right]\!\!\right] = 0\,, \tag{51}$$

$$\left[\!\!\left[\left(u - \frac{2}{3}\right)\sigma u + \frac{\sigma a}{\lambda_D^3}\right]\!\!\right] = 0\,, \tag{52}$$

$$\left[\!\!\left[\left(u - \frac{2}{3}\right)\sigma\Lambda\right]\!\!\right] = 0\,, \tag{53}$$

$$\left[\!\!\left[\left(u - \frac{2}{3}\right)\sigma\left[\frac{u^2}{2} + \left(\mu^2 - \frac{5}{2}\right)\frac{\Lambda^2}{2\lambda_D^3}\right] + \frac{5}{2}\,\frac{\sigma a}{\lambda_D^3}\left(u - \frac{2}{5}\right)\right]\!\!\right] = 0\,. \tag{54}$$

A solution to system (51)–(54) can be found if the position of the discontinuity λ_D is known:

$$u_2 = \frac{1}{2} + \left(u_1 - \frac{2}{3}\right)^{-1}\frac{5}{4}\,\frac{a_1}{\lambda_D^3} + \frac{u_1}{4}\,, \tag{55}$$

$$\sigma_2 = \frac{u_1 - 2/3}{u_2 - 2/3}\,\sigma_1\,, \tag{56}$$

$$a_2 = \frac{\sigma_1}{\sigma_2}\left[\left(u_1 - \frac{2}{3}\right)^2\frac{3}{4}\,\lambda_D^3 - \frac{a_1}{4}\right], \tag{57}$$

$$\Lambda_2 = \Lambda_1\,. \tag{58}$$

Comparing the expression for the first singular point (41) and the velocity of discontinuity (55), we see that this singular point corresponds to the gas velocity equal to the SW velocity, i.e., to an impossible situation. Thus, the first singular point is not realized.

The second singularity, Eqn (42), is associated with the sonic point (44). It is easy to verify by direct substitution into Eqns (55)–(57) that the passage through this singular point is not accompanied by a discontinuity or infinite values of hydrodynamic quantities. On the other hand, the derivative of the density at this point with respect to λ becomes infinite. Thus, point (42) is a caustic-type singularity.

The SW intensity depends on its self-similar coordinate λ_D, which cannot be determined analytically. The gas temperature behind the SW depends on the self-similar coordinate rather strongly, $\sim \lambda_D^3$ (see (57)), so approximate estimates for the self-similar coordinate (for example, based on the energy conservation law) are clearly not sufficient. Based on this, we performed further numerical analysis.

3.2 Numerical model and calculation results

We used in the numerical model the Lagrangian form of Eqns (14)–(17). It is convenient to introduce instead of the radial coordinate r the mass Lagrangian coordinate q that satisfies the relation $\mathrm{d}q = r\rho\,\mathrm{d}r$. As a result of such a replacement, the system of equations takes the following form:

$$\frac{\mathrm{d}}{\mathrm{d}t}\left(\frac{1}{\rho}\right) = \frac{\partial(rv_r)}{\partial q}\,, \tag{59}$$

$$\frac{\mathrm{d}v_r}{\mathrm{d}t} = -r\,\frac{\partial P}{\partial q} + \frac{v_\phi^2}{r} - (1 - \xi)\,\frac{GM}{r^2}\,, \tag{60}$$

$$\frac{\mathrm{d}v_\phi}{\mathrm{d}t} = -\frac{v_r v_\phi}{r}\,, \tag{61}$$

$$\frac{\mathrm{d}E}{\mathrm{d}t} = -P\,\frac{\partial(rv_r)}{\partial q}\,, \tag{62}$$

$$\frac{\mathrm{d}r}{\mathrm{d}t} = v_r\,. \tag{63}$$

Instead of the equation for density (59), an equivalent equation may be used:

$$\frac{1}{\rho} = r\,\frac{\partial r}{\partial q}\,. \tag{64}$$

Also, the law of conservation of angular momentum $\mathrm{d}(rv_\phi)/\mathrm{d}t = 0$ follows from Eqns (61) and (63).

The quantities in Eqns (59)–(63) were reduced to a dimensionless form according to the following scheme: $r/r_* \mapsto r$, $v/c_* \mapsto v$, $t/(r_*/c_*) \mapsto t$, $\rho/\rho_* \mapsto \rho$, $P/(\rho_* c_*^2) \mapsto P$,

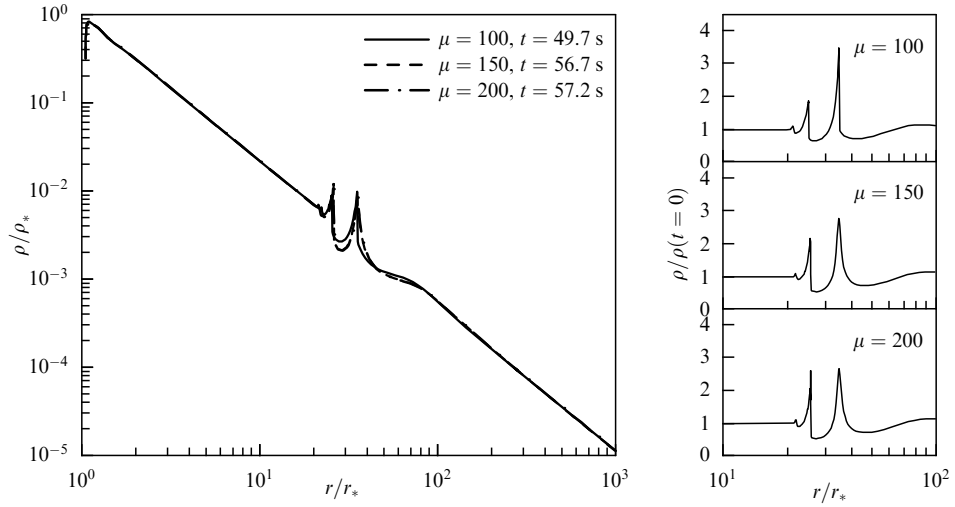

Figure 2. Radial density distribution in models with various values of the Mach number μ. The moments of time are chosen in such a way that the positions of the shock wave coincide in all cases.

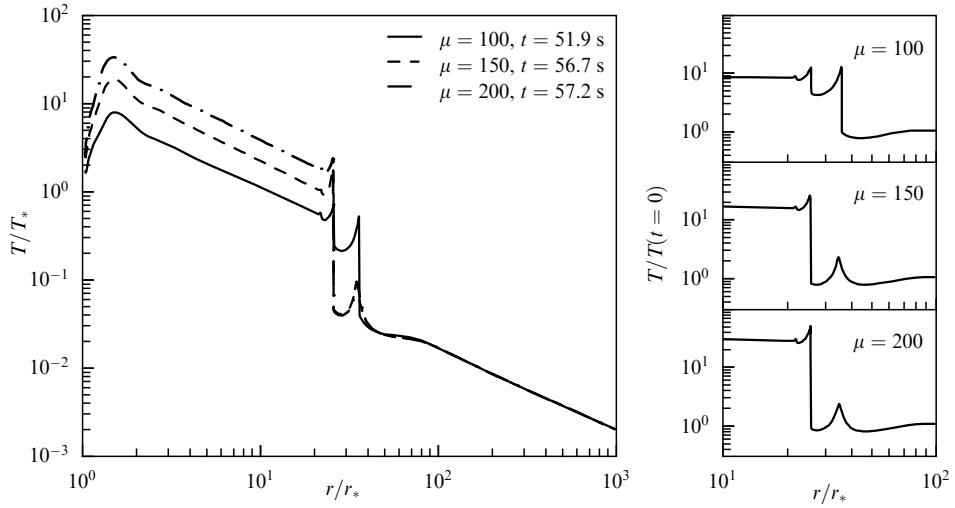

Figure 3. Radial temperature distribution. Same notations as in Fig. 2.

$E/c_*^2 \mapsto E$, $q/(r_*^2\rho_*) \mapsto q$. In a dimensionless formulation, the problem has only two parameters: ξ and μ (see Eqn (21)). However, the physical formulation of the problem is determined by five quantities: the turbulence parameter α, the dimensionless mass m, the dimensionless accretion rate $\dot{m}$, the ratio of the temperatures in the center and on the surface of the disk (heat transport mechanism) $f_{\rm ht}$, and the fraction of the mass lost ξ (see Section 2). In a realistic range of values of the parameters, $0.1 < \dot{m} < 1$, $2 < f_{\rm ht} < 10$, for $m = 50$, the characteristic values of the temperature T_* (12) fall within the range of $4 \times 10^6 - 4 \times 10^7$ K. This range corresponds to the range of Mach numbers $\mu = 85 - 254$.

A numerical scheme was developed for system (59)–(63) based on the Samarskii and Popov method [41, 42], the details of which are described in [22]. We only note that in this scheme not only are difference analogues of the laws of conservation of mass, momentum, and energy fulfilled, but also additional relations describing the balance for certain types of energy hold valid. In addition, the law of conservation of angular momentum is exactly fulfilled in the scheme.

We explored three numerical models with $\mu = 100$, 150, and 200.We used power profiles (10) and (11) as the initial distributions. The dependences of dimensionless density, temperature, and radial and tangential velocities on r/r_* for three values of μ are shown in Figs 2–5. All three calculations exhibited qualitatively similar flow properties: one or two shock waves emerge in the central region of the disk, depending on the value of μ. The wave propagates through the disk with deceleration. The density on the SW undergoes a jump by a factor of three or more, and the temperature of about 7.5–27 times compared with the initial value (Table 2). The radial velocity oscillates with an amplitude of the order of the speed of sound or more. The flow characteristics in front of the SW remain virtually constant during the entire calculation interval.

Table 2. Some characteristics of disks: Mach number μ, temperature T_* in the central part of the unperturbed disk, temperature jump $T/T(t=0)$ behind the shock wave.

μ	T_*, K	$T/T(t=0)$
100	2.7×10^7	7.5
150	1.2×10^7	15.5
200	0.43×10^7	27

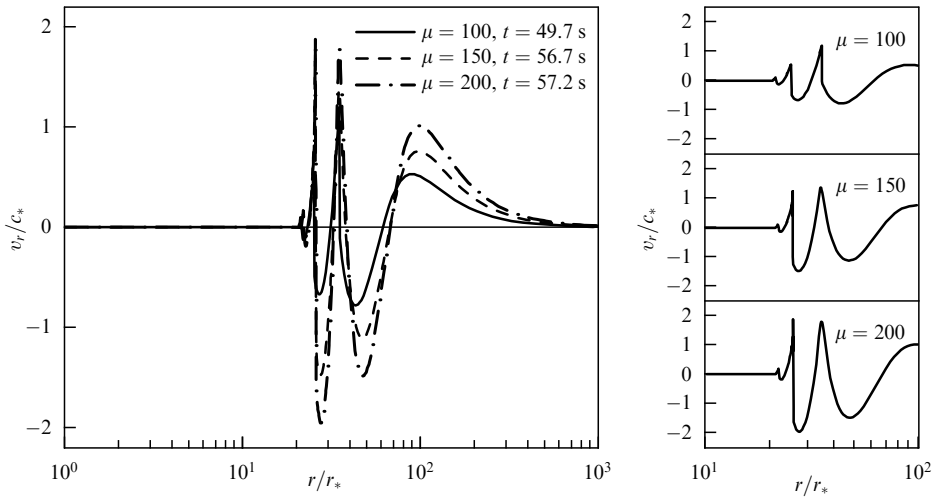

Figure 4. Radial distribution of radial velocity. Same notations as in Fig. 2.

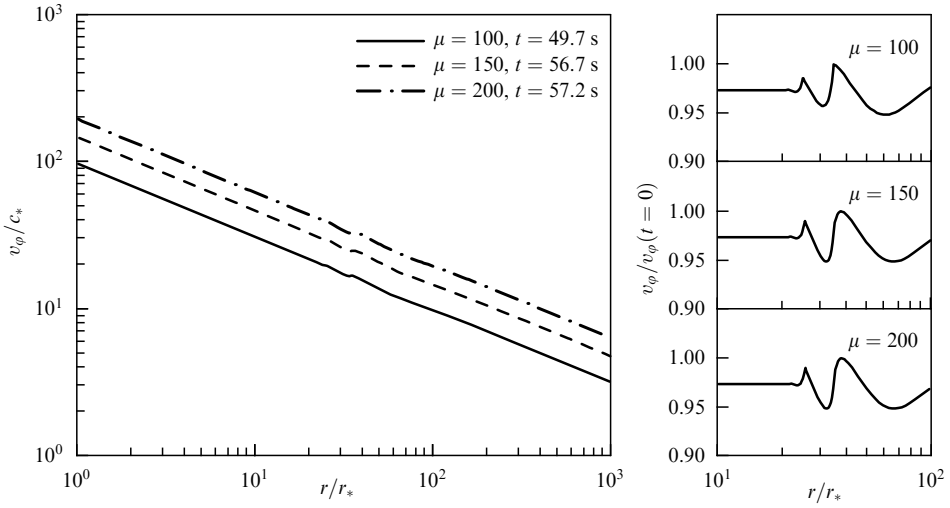

Figure 5. Radial distribution of tangential velocity. Same notations as in Fig. 2.

The gas flow in the disturbed part of the disk is a combination of large-amplitude waves of density, temperature, and radial velocity. For $\mu = 200$ and 150, at the outer boundary of the perturbed region, one shock wave emerges with a precursor (caustic on the distribution of density and temperature); at $\mu = 100$, the caustic turns into an SW. We also performed calculations for the Mach numbers $\mu = 50$ and $\mu = 10$ (not shown in the figures). It is noteworthy that for small values of μ there is only one shock wave with a precursor in the disk.

It turns out that the SW position as a function of time does not depend on the Mach number in the disk and allows a simple approximation that functionally reproduces the self-similar law of SW propagation that we obtained above:

$$r_D = 1.76\, r_* t^{2/3}\,. \tag{65}$$

We can derive from this equation an expression for the SW velocity similar to (55):

$$D = \frac{\mathrm{d}r_D}{\mathrm{d}t} = 1.2\, r_*\, t^{-1/3} = 1.59\, r_* \left(\frac{r_D}{r_*}\right)^{-1/2}. \tag{66}$$

Figure 6 shows the SW trajectories. The mismatch between the plots for $\mu = 100$ and other charts is due to the fact that the program code searches for the discontinuity from the side of the right-hand (external) part of the computational domain. At the same time, two shock waves emerge for this value of the Mach number (see Fig. 3), and the trajectory of the internal SW coincides with that for $\mu = 150$ and $\mu = 200$.

The shock wave arising in the disk leads to a 7.5–27-fold temperature increase, depending on the Mach number (see Fig. 3 and Table 2). As a result, the gas in the inner part of the disk is heated to a temperature of 2×10^8 K, which corresponds to a thermal energy per particle of about 17.2 keV. Under conditions of a nonmagnetic accretion disk, the electromagnetic radiation spectrum in this energy range is determined by two processes [43]: bremsstrahlung of electrons and Compton scattering. The latter can lead to an increase in photon energy and distortion of the spectrum: a decrease in intensity at the frequencies of the Planck maximum and the emergence of a 'tail' in the high-energy region [44, 45]. However, spectrum comptonization is only effective if the layer through which the radiation passes is transparent [43, 45]. We estimate the optical thickness of the disk at the radiation frequency ν as $\tau_\nu = (\kappa_\nu^{\mathrm{ff}} + \kappa^{\mathrm{es}})\Sigma$.

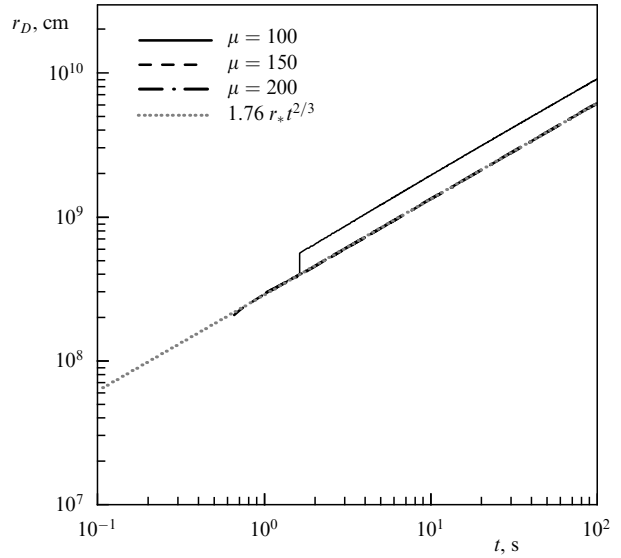

Figure 6. Position of a shock wave as a function of time. The dotted line shows the approximation.

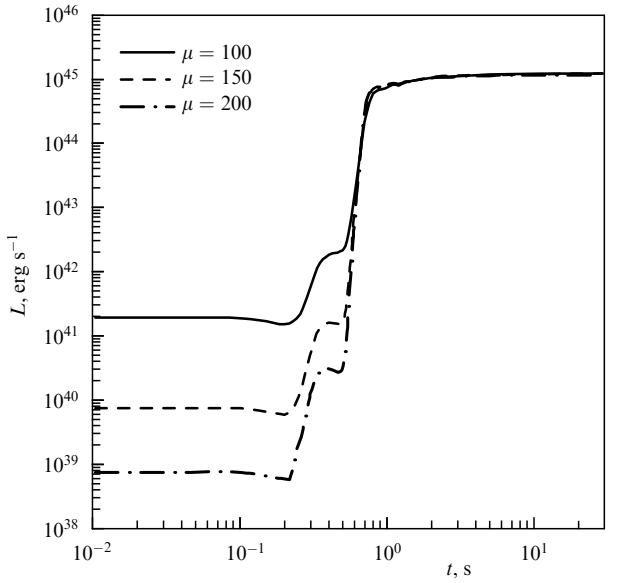

Figure 7. Bolometric light curves in models with various Mach numbers.

Substituting the expression for the absorption cross sections, for example, from [44], we can show that in the central part of the disk ($\rho \sim 1$ g cm^{-3}, $T \sim 10^8$ K, $H \sim 10^6$ cm) the optical thickness across the entire spectrum is much greater than unity and at wavelengths of less than 10 nm is determined by Compton scattering. This property also holds in the outer parts of the disk. The distortion of the spectrum in an optically thin layer near the disk surface is also insignificant, since the ratio of the geometric thickness of this layer to the disk thickness (it can be estimated as τ_ν^{-1}) is negligible at all frequencies. Thus, it can be assumed that radiation from the surface of the disk has a Planck spectrum everywhere.

Figure 7 shows the change in the bolometric luminosity of the disk versus time calculated as

$$L(t) = 2\pi \int_{r_*}^{\infty} \mathrm{d}r\, r\, \sigma_{\mathrm{SB}} T_{\mathrm{s}}^4(t, r)\,. \tag{67}$$

It is noteworthy that different values of the parameter μ eventually resulted in the same disk luminosity, of the order of 10^{45} erg s^{-1}.

It should be recalled that we consider in this section the hydrodynamic model without taking into account radiative processes. Figures 3 and 7 show that the gas temperature remains almost unchanged after the shock jump. This approximation obviously fails at large times, since the radiative cooling process should lead to cooling of the disk after SW passage and the gradual establishment of a new equilibrium state in which the energy emission rate is equal to the viscous heating rate. We estimate the radiative cooling time as the time of radiation diffusion (for $\tau_{\mathrm{R}} \sim 10^5 - 10^6$):

$$t_{\mathrm{rad}} \sim \tau_{\mathrm{R}}\, \frac{H}{c} \gtrsim 3 - 30\ \mathrm{s}\,. \tag{68}$$

A more general expression has the form (at such temperatures, the cross section κ^{ff} does not contribute to the absorption)

$$t_{\mathrm{rad}} = \frac{2\kappa^{\mathrm{es}} \rho_* H_*^2}{c} \left(\frac{r}{r_*}\right)^{3-(k_{\mathrm{d}}+k_{\mathrm{t}})}\,. \tag{69}$$

The characteristic width of the hot region behind the SW can be estimated as

$$\Delta r_D = D t_{\mathrm{rad}}\,, \tag{70}$$

where D is the SW velocity (66). Substituting r_D in place of r in Eqns (69) and (70), we can see that the width of the hot region Δr_D weakly depends on time (as $t^{-0.075}$) and may be approximately expressed as

$$\Delta r_D \approx 42.4\, r_*\,. \tag{71}$$

This implies that the effects of radiative cooling should not significantly change the temperature distribution shown in Fig. 3. The time during which the temperature decreases to its original value is estimated as follows:

$$t_{\mathrm{cool}} = t_{\mathrm{rad}}\, \frac{T}{T\big|_{t=0}}\,. \tag{72}$$

If the temperature behind the SW increases by 7.5–27 times, then the decay time of the light curve will be from 4 to 14 min. The calculation of bolometric light curves showed that the luminosity of the disk increases by 4–6 orders of magnitude, up to 10^{45} erg s^{-1}, a value that corresponds to an absolute stellar magnitude of -23.8^{m}. The disk luminosity is determined by the temperature of the gas near the inner boundary. At temperatures $\gtrsim 10^8$ K, blackbody radiation is concentrated primarily in the hard X-ray and gamma-ray spectral ranges. It is noteworthy that the bolometric luminosity in this model does not depend on the initial temperature of the disk, but is apparently determined by the mass of the accretor and the fraction of the mass lost.

4. Accounting for radiation pressure

A disadvantage of the model considered in Section 3.2 is that the thermal structure of the equilibrium disk and its dynamics only depend on gas pressure, while radiation pressure can play a significant role. It was assumed in addition that heat transport in the vertical direction in the disk is convective, while the temperature of the equilibrium disk is normalized

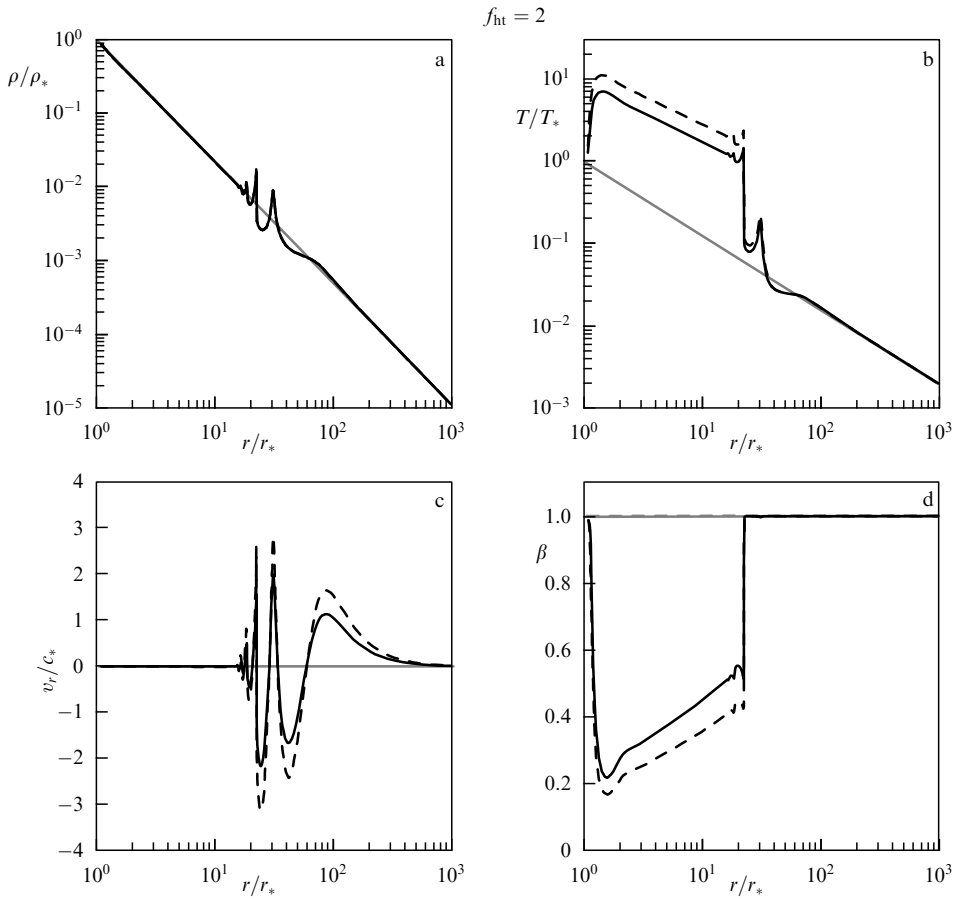

Figure 8. Distribution of (a) density, (b) temperature, (c) radial velocity, and (d) relative gas pressure for two convective disk models with consideration for radiation pressure: $\dot{m} = 1$ (solid lines) and $\dot{m} = 0.05$ (dashed lines) at moment of time $t \approx 30$ s. Gray curves show corresponding distributions for unperturbed disks.

based on the radiative heat transport mechanism, as is done in the original study [27]. As a result, the disk luminosity could be overestimated. We tried below to correctly take into account the contribution of the radiation pressure to the disk dynamics. We performed two series of calculations: with disks that have a radiative structure and with those with a convective structure, with various accretion rates.

4.1 Numerical model

The total pressure and internal energy of a gas together with the radiation are respectively expressed as

$$P = A\rho T + \frac{aT^4}{3}\,, \tag{73}$$

$$E = \frac{AT}{\gamma - 1} + \frac{aT^4}{\rho}\,, \tag{74}$$

where A is the gas constant, the adiabatic index $\gamma = 5/3$, and $a = 4\sigma_{SB}/c = 7.56 \times 10^{-15}$ erg cm^{-3} K^{-4}. To estimate the role of radiation pressure, we introduce the parameter β that describes the contribution of gas pressure to the total pressure at the inner boundary of the disk:

$$P_{g*} = \beta P_*\,, \qquad P_{r*} = (1-\beta)\,P_*\,, \tag{75}$$

where P_{g*}, P_{r*}, and P_* are the gas, radiative, and total pressures, respectively, at $r = r_*$. We assume that the profiles of equilibrium distribution of gas temperature and density are power functions (see (10) and (11)). The distribution of pressure and specific angular momentum at the initial moment of time has the following form:

$$P_0 = r_* c_*^2 \left[\beta\left(\frac{r}{r_*}\right)^{-k_d-k_t} + (1-\beta)\left(\frac{r}{r_*}\right)^{1-4k_t}\right], \tag{76}$$

$$L_0 = r_* c_* \left[\mu^2 - (k_d + k_t)\,\beta\left(\frac{r}{r_*}\right)^{1-k_t} - 4k_t(1-\beta)\left(\frac{r}{r_*}\right)^{1+k_d-4k_t}\right]^{1/2}\left(\frac{r}{r_*}\right)^{1/2}. \tag{77}$$

We take typical values of gas parameters near the inner boundary of the disk: $\rho = 1$ g cm^{-3} and $T = 10^7$ K. Under these conditions, the contribution of radiation pressure is insignificant: $\beta = 0.98$. If, however, the temperature significantly increases as a result of, for example, shock compression, the role of radiation in the gas dynamics becomes crucial. In particular, for $T = 10^8$ K, we obtain $\beta = 0.06$.

Similar to the previous model [22], where gas pressure alone was taken into account, we calculated the adiabatic gas flow in the middle plane of the disk. To solve the system of equations (59)–(63) taking into account the equations of state of pressure and internal energy in the form of (73) and (74), a numerical scheme based on the Samarskii–Popov method [41, 42] has been developed. The solution was completely determined by the following parameters: indices of initial

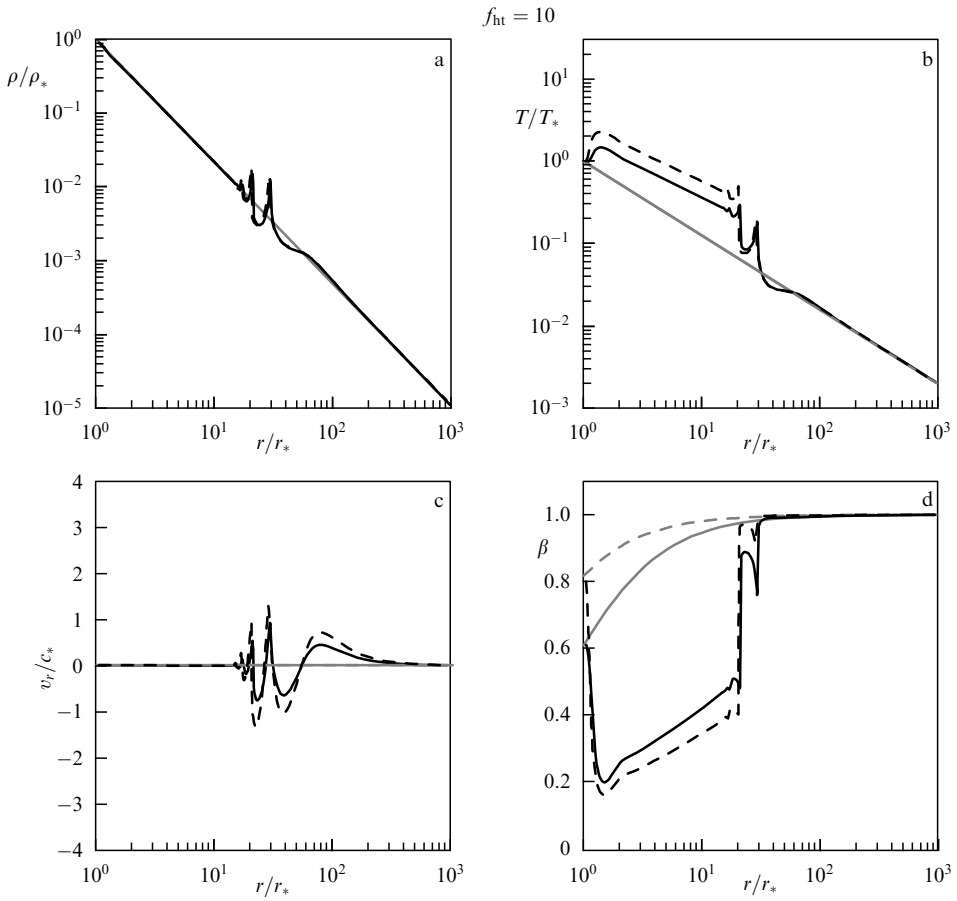

Figure 9. Same as in Fig. 8, but for radiative discs. The distributions correspond to the moment $t \approx 26$ s.

profiles $k_t = 9/10$ and $k_d = 33/20$; fraction of mass lost $\xi = 0.05$; pressure parameter β; and the Mach number on the inner boundary $\mu = [GM/(r_* c_*^2)]^{1/2}$, where $c_*^2 = P_*/\rho_*$. The parameters β and μ depend on T_* and ρ_*, which are determined by the dimensionless accretor mass m, the dimensionless accretion rate $\dot{m}$, the turbulence parameter α, and the temperature drop f_{ht} on the vertical disk scale that depends on the heat transport mechanism (9). We performed calculations for convective and radiative disk models with accretion rates $\dot{m} = 0.05$ and $\dot{m} = 1$. In all the calculations, the values $m = 55$ and $\alpha = 0.01$ were taken. The values of key parameters and scale values are given in Table 3.

Table 3. Characteristics of numerical models of convective disks (2nd and 3rd columns, $f_{ht} = 2$) and radiative disks (4th and 5th columns, $f_{ht} = 10$).*

Parameter	$f_{ht} = 2$ (convective disk)		$f_{ht} = 10$ (radiative disk)	
$\dot{m}$	0.05	1.0	0.05	1.0
ρ_*, g cm^{-3}	0.35	1.2	0.35	1.2
T_*, K	3.5×10^6	7.4×10^6	1.7×10^7	3.7×10^7
c_*, cm s^{-1}	2.4×10^7	3.5×10^7	5.9×10^7	1.0×10^8
t_*, s	6.8	4.7	2.7	1.6
μ	278	191	112	67
β	0.9982	0.9948	0.8128	0.6034
max T, K	3.9×10^7	5.1×10^7	3.9×10^7	5.3×10^7
L, erg s^{-1}	3.2×10^{42}	9.9×10^{42}	5.5×10^{39}	1.9×10^{40}
min β	0.1681	0.2190	0.1634	0.2016

* The upper part of the table displays parameters of the initial disks. All other parameters are the same for all disks: $r_* = 1.6 \times 10^8$ cm, $2\pi/\Omega_* = 2.4 \times 10^{-2}$ s, $\xi = 0.05$, $\alpha = 0.01$. The lower three rows in the table contain the maximum temperature across the disk, luminosity, and the minimum value of β at the time the calculation was completed.

4.2 Calculation results

Figure 8 shows the results of calculations of a convective disk at a time point of approximately 30 s. Within a short time (several tenths of a second), an SW emerged in the disk, behind the front of which the temperature increased by more than an order of magnitude. The temperature jump is most sensitive to the value of the Mach number μ, since the force caused by the imbalance of gravity and rotation is proportional to μ^2 (see Eqn (60)). In a radiative disk, the speed of sound is several times higher than in a convective one (see Table 3); therefore, the response of the disk to mass loss by the accretor is less pronounced. For example, the temperature behind the SW increases by 4–6 times, depending on the accretion rate (Fig. 9).

In all calculations, the temperature behind the shock wave front increases to approximately $(4-5) \times 10^7$ K (Fig. 10). At this temperature and density $\rho \lesssim 1$ g cm^{-3}, the radiation pressure prevails over the gas pressure. The relative contribution of gas pressure to total pressure at the point of maximum temperature is about 0.2 (β in Figs 8 and 9). It can be shown that in this case the heat capacity of the 'mixture' of gas and radiation increases. As a result, the temperature jump behind the SW decreases. While in a disk with pure gas pressure the jump magnitude increases with an increase in the Mach number as μ^2 [22], an account of radiative pressure yields weaker dependences: $(\max T)/T_* \propto \mu^{1.28}$ for the convective

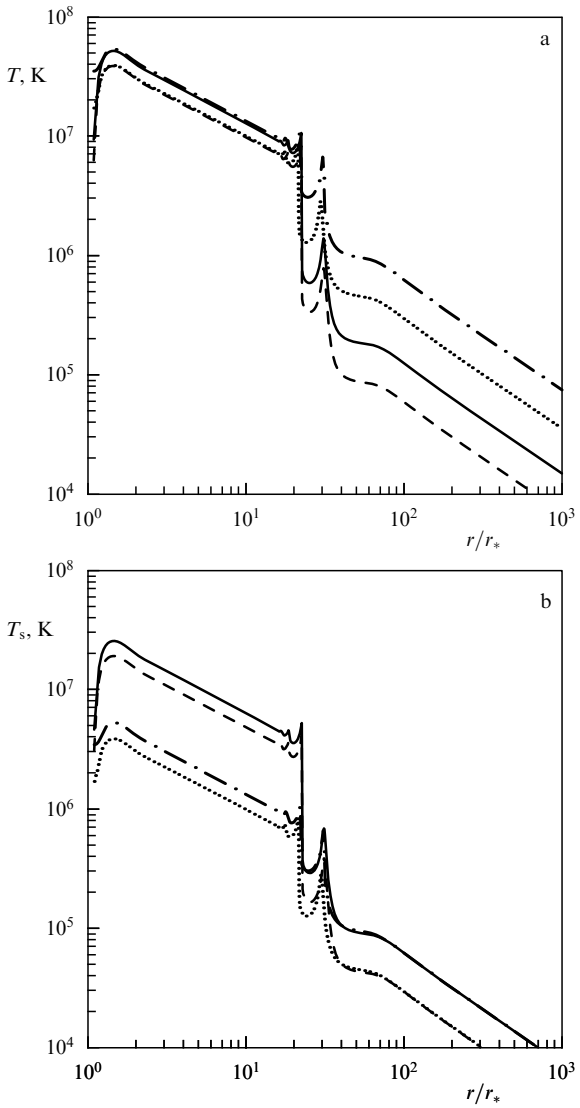

Figure 10. Temperature distribution for four models taking into consideration radiation pressure: (a) in the middle plane of the disk and (b) on the surface of the disk. The solid line is for a convective disk ($f_{\rm ht} = 2$) with a high accretion rate ($\dot{m} = 1$). The dashed line is for a convective disk with a low accretion rate ($\dot{m} = 0.05$). The dashed-dotted line is for a radiative disk ($f_{\rm ht} = 10$) with a high accretion rate. The dotted line is for a radiative disc with a low accretion rate.

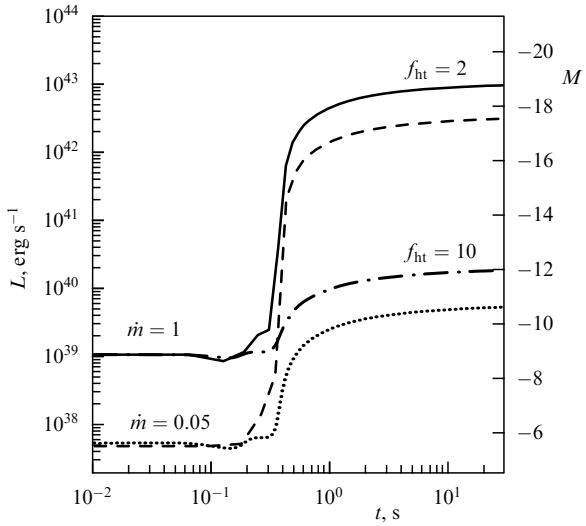

Figure 11. Light curves for four models taking into consideration radiation pressure. Same notations for the curves as in Fig. 10.

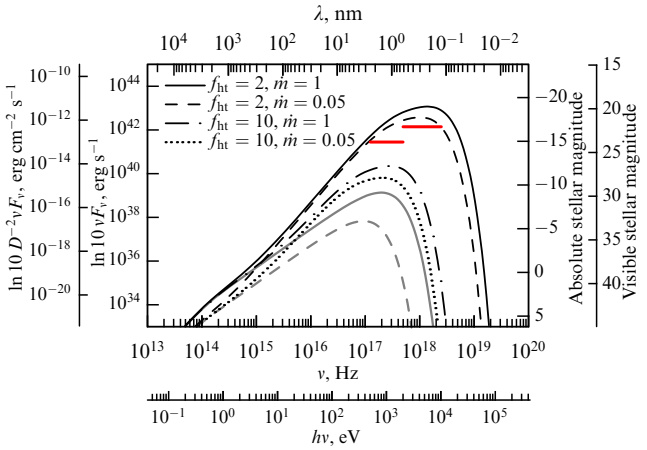

Figure 12. Electromagnetic radiation spectra for models that take into account radiation pressure, in units of luminosity per unit logarithmic frequency interval. Internal vertical scales: luminosity (left) and absolute bolometric stellar magnitude (right). External vertical scales correspond to a source located at a distance of 540 Mpc: flux through a unit detector area (left) and visible stellar magnitude (right). Notations for the black lines are the same as in Fig. 10. The gray curves display spectra of unperturbed disks. Horizontal bars show the lower sensitivity limits of the EPIC-MOS and EPIC-PN detectors of the XMM-Newton observatory (5σ level at an exposure of 10^3 s) [46].

disk and $(\max T)/T_* \propto \mu^{0.92}$ for the radiative one (see Table 3).

For the same accretion rate, the surface temperature distribution of the unperturbed disk is the same for both the convective and radiative heat transport mechanisms (see Fig. 10). After the SW passage, convective disks exhibit both a greater relative change in temperature and a greater absolute value of it. The reason is that the radiation pressure cannot be ignored even in unperturbed radiative disks (see Fig. 9), and it has a stronger effect on the dynamics of gas compression by the shock wave than in the case of convective disks.

Depending on the thermal structure and accretion rate, the initial temperature inside the disks in its hottest, central region varied within the same order of magnitude: from 3.5×10^6 K for convective disks to 3.7×10^7 K for radiative ones. However, the maximum temperature inside the disks after the SW passage was approximately the same, $(3.9-5.3) \times 10^7$ K (see Table 3 and Fig. 10). This implies that convective disks are more efficient in converting the perturbation energy into the internal energy of the gas, apparently because their inner layers are colder than those of radiative disks, and the radiation pressure plays a lesser role in the dynamics of convective disks. Therefore, a larger fraction of the perturbation energy is transformed in convective disks into gas compression energy, which is reflected in a larger increase in temperature.

We used the calculated temperature profiles to determine light curves (Fig. 11). After an SW emerges and advances into the interior of the disk, the luminosity for models with convective energy transport increases by 4–5 orders of magnitude, depending on the accretion rate, to reach $3 \times 10^{42}-10^{43}$ erg s^{-1}, or an absolute stellar magnitude of

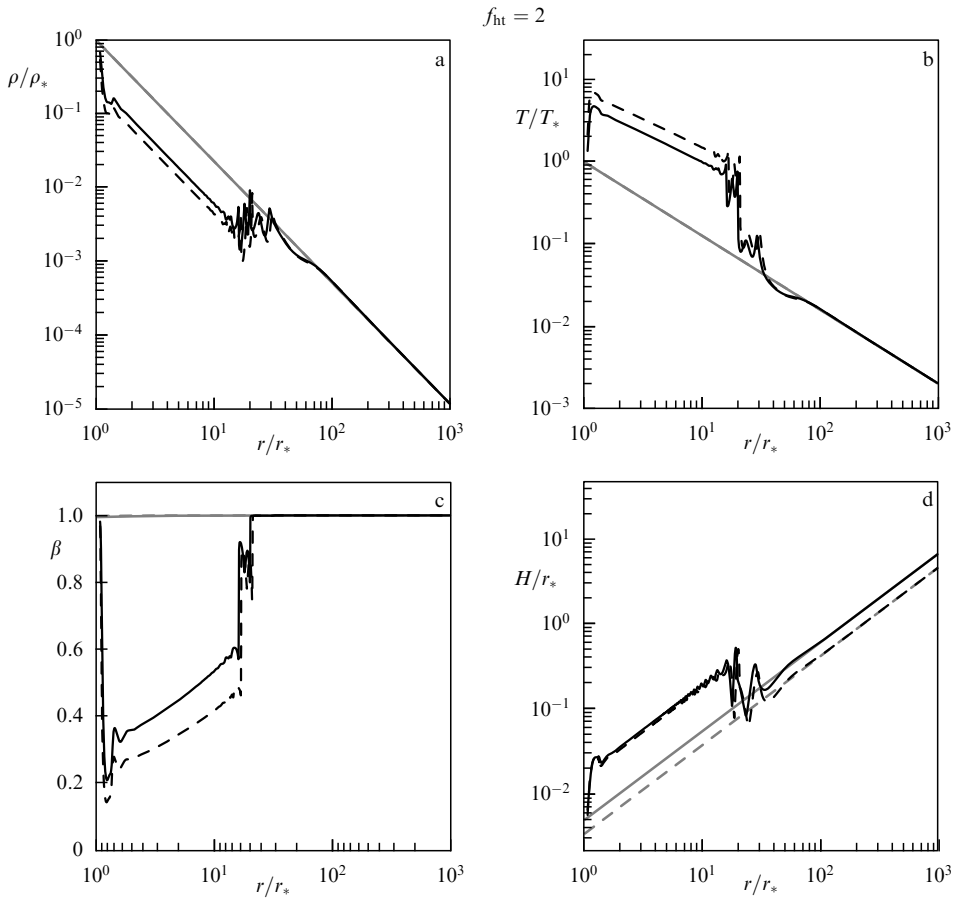

Figure 13. Distribution of (a) density, (b) temperature, (c) relative gas pressure, and (d) disk thickness for two convective disk models with vertical expansion taken into account: $\dot{m} = 1$ (solid curves) and $\dot{m} = 0.05$ (dashed curves). The gray curves show the corresponding distributions for unperturbed disks.

$-(17.5-19)$. For radiative models, the luminosity increases by 1–2 orders of magnitude, to $5 \times 10^{39} - 2 \times 10^{40}$ erg s^{-1}, reaching a stellar magnitude of $-(10.5-12)$. Thus, convective discs at the same accretion rate provide a greater increase in luminosity (by about three orders of magnitude) than radiative ones.

The spectral density of the radiation flux (on one side of the disk) was calculated using the Planck function:

$$F_\nu = 2\pi^2 \int_{r_*}^{\infty} \mathrm{d}r\, r B_\nu \left[T_{\rm s}(r)\right] . \qquad (78)$$

Figure 12 shows the spectra at a time point of approximately 30 s (as in Fig. 10). The fluxes are given in absolute units and for a source located at a distance $D = 540$ Mpc, which corresponds to the source GW170814 [23] (to do so, the flux was divided by D^2).

As can be seen from Fig. 12, the maximum radiation flux of radiative disks lies in the range of soft X-ray radiation, $\gtrsim 10^2 - 10^3$ eV, while a significant part of the flux from convective disks lies in the hard X-ray range, 5–30 keV. Disks with convective heat transport are above the sensitivity threshold of the EPIC (European Photon Imaging Camera) instrument of the XMM (X-ray Multi-Mirror)-Newton observatory (5σ levels are shown for an exposure time of 10^3 s) [46]. For the radiative discs to be observable, the distance to a source like GW170814 should be at least three times smaller.

The flux from the convective disk in the near and intermediate ultraviolet ranges (frequency of $\sim 10^{15}$ Hz) is 2–10 times larger. In the extreme ultraviolet range (10–100 eV), the brightness can increase by two orders of magnitude.

The accretion disk model considered in this section does not take into account that, due to heating by a shock wave, the disk can expand vertically, as a result of which the gas temperature will decrease due to adiabatic cooling. This temperature can be estimated as follows. After shock heating, the equilibrium half-thickness of the disk should increase by a factor of two to three: $H/H_* \sim [(\max T)/T_*]^{1/2} \approx 2-3$, and as a result of adiabatic cooling, the temperature should be more than halved: $(H/H_*)^{1-\gamma} \approx 0.5-0.6$. Accordingly, the decrease in luminosity should be up to an order of magnitude. We consider in Section 5 the effects caused by disk expansion in the vertical direction.

5. Accounting for vertical expansion

After the merger of a binary BH, the gravitational force that acts on the gas from the accretor decreases, and gas temperature rises due to shock heating. As a result, the previous vertical scale of the disk H_* is no longer an equilibrium one. The relaxation of gas in the vertical direction to a new equilibrium state occurs during a time of the order of the sonic time interval, $H_*/c_* \sim \Omega_*^{-1}$, while the luminosity in the disk increases over a much longer time, of

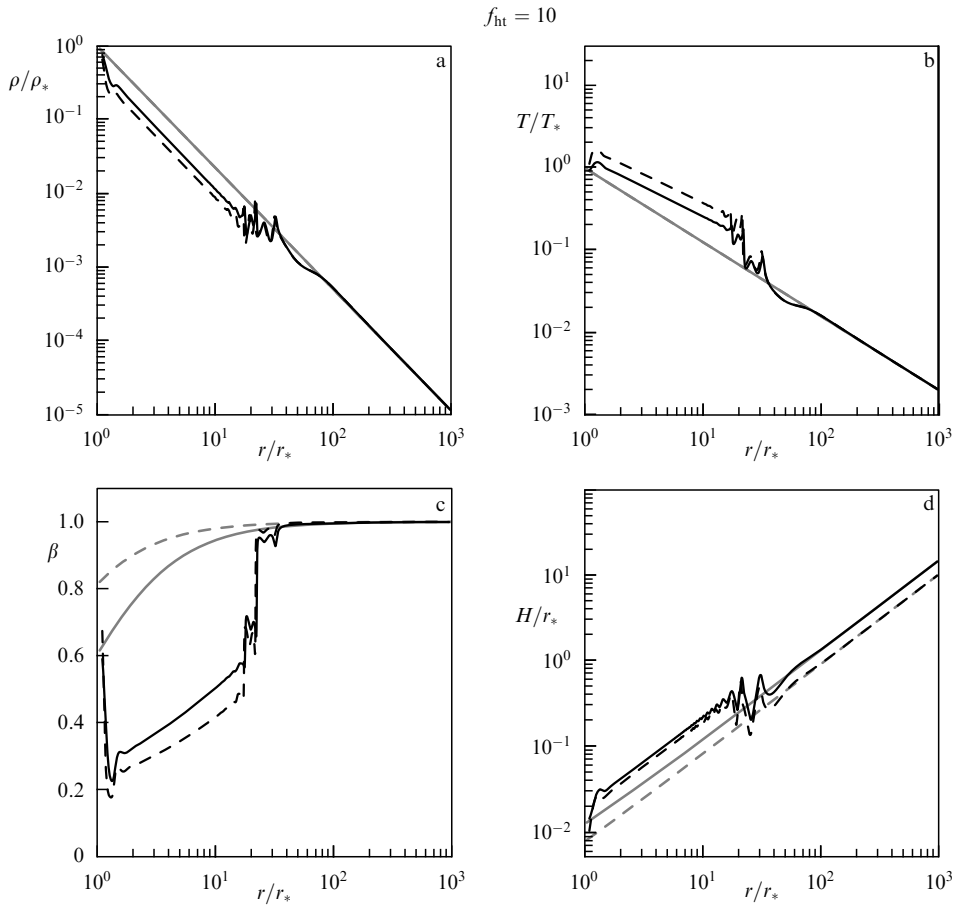

Figure 14. Same as in Fig. 13 but for radiative discs.

the order of $t_* = r_*/c_* = r_*/(H_*\Omega_*) \sim \mu/\Omega_*$. A consequence of the rapid gas expansion in the vertical direction is the adiabatic cooling of the gas that should somewhat reduce the intensity of the electromagnetic response of the accretion disk.

5.1 Numerical model

The disks described by the α-model are geometrically thin: the ratio of the half-thickness to the radius is $H/r \sim \mu^{-1} \sim 0.01$ (see Section 3). For this reason, a detailed description of the vertical structure of a disk is hardly needed for studying the effects of shock heating and rapid adiabatic cooling.

We adopt as a basic assumption the uniform gas expansion/compression law:

$$v_z(t, r, z) = \psi(t, r)\, z\,. \tag{79}$$

Given the vertical motion of the gas, the equations of continuity and energy change:

$$\frac{\mathrm{d}\rho}{\mathrm{d}t} = -\rho\,\frac{1}{r}\,\frac{\partial(rv_r)}{\partial r} - \rho\psi\,, \tag{80}$$

$$\frac{\mathrm{d}E}{\mathrm{d}t} = -\frac{P}{\rho}\,\frac{1}{r}\,\frac{\partial(rv_r)}{\partial r} - \frac{P}{\rho}\,\psi\,. \tag{81}$$

The Euler equations for the radial and azimuthal velocity do not change:

$$\frac{\mathrm{d}v_r}{\mathrm{d}t} = -r\,\frac{\partial P}{\partial q} + \frac{v_\phi^2}{r} - (1-\xi)\,\frac{GM}{r^2}\,, \tag{82}$$

$$\frac{\mathrm{d}v_\phi}{\mathrm{d}t} = -\frac{v_r v_\phi}{r}\,, \tag{83}$$

$$\frac{\mathrm{d}r}{\mathrm{d}t} = v_r\,. \tag{84}$$

However, the equation for vertical velocity is added:

$$\frac{\mathrm{d}v_z}{\mathrm{d}t} = -\frac{1}{\rho}\,\frac{\partial P}{\partial z} - (1-\xi)\,\frac{GM}{r^3}\,z\,, \tag{85}$$

from which an equation for ψ may be derived. To do so, we write

$$\frac{\mathrm{d}v_z}{\mathrm{d}t} = \frac{\mathrm{d}\psi}{\mathrm{d}t}\,z + \psi\,\frac{\mathrm{d}z}{\mathrm{d}t} = \left(\frac{\mathrm{d}\psi}{\mathrm{d}t} + \psi^2\right) z\,. \tag{86}$$

On the other hand, we have the approximation

$$-\frac{1}{\rho}\,\frac{\partial P}{\partial z} \approx \frac{P}{\rho H^2}\,z\,. \tag{87}$$

Using Eqns (85)–(87), we obtain

$$\frac{\mathrm{d}\psi}{\mathrm{d}t} = -\psi^2 + \frac{P}{\rho H^2} - (1-\xi)\,\frac{GM}{r^3}\,. \tag{88}$$

Finally, the half-thickness of the gas disk at a given radius satisfies the relation

$$\frac{\mathrm{d}H}{\mathrm{d}t} = \psi H\,. \tag{89}$$

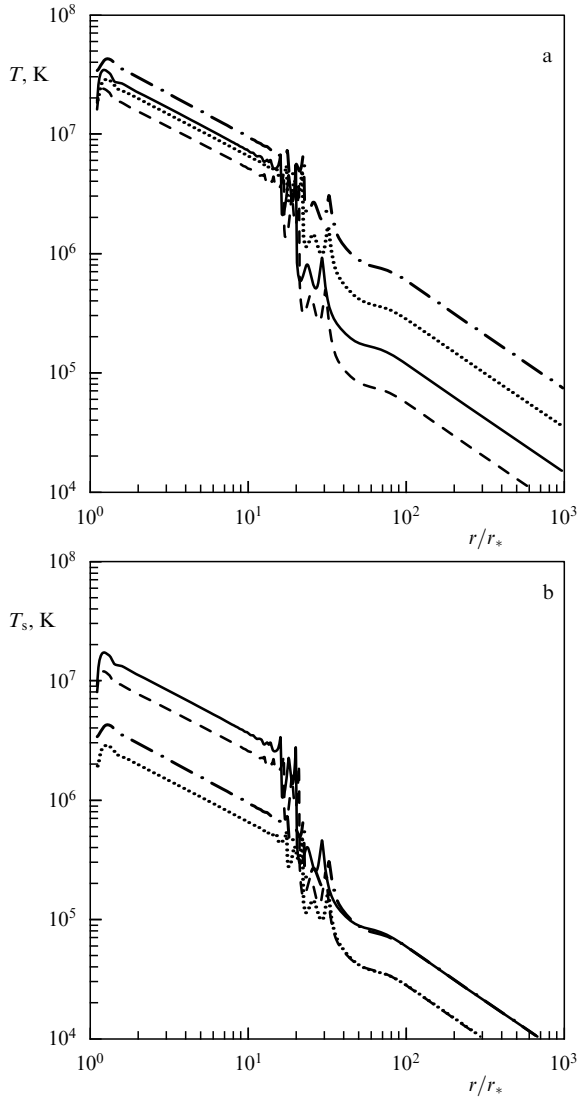

Figure 15. Temperature distribution for four models allowing for vertical expansion: (a) in the middle plane of the disk and (b) on the surface of the disk. The solid line is for a convective disk ($f_{ht} = 2$) with a high accretion rate ($\dot{m} = 1$). The dashed curve is for a convective disk with a low accretion rate ($\dot{m} = 0.05$). The dashed-dotted curve is for a radiative disk ($f_{ht} = 10$) with a high accretion rate. The dotted curve is for a radiative disc with a low accretion rate.

At the initial moment $t = 0$, the disk is in equilibrium:

$$H\big|_{t=0} = \left[\frac{r^3}{GM}\frac{P}{\rho}\bigg|_{t=0}\right]^{1/2}, \tag{90}$$

$$\psi\big|_{t=0} = 0\,. \tag{91}$$

Thus, the evolution of the gas disk in this model is described by the system of equations (80)–(84), (88), and (89) with the initial conditions (10), (11), (76), (77), (90), and (91). To calculate the model, a numerical scheme based on the Samarskii–Popov method has been developed again. As described in Section 4, calculations were performed for convective and radiative models of disks with accretion rates $\dot{m} = 0.05$ and $\dot{m} = 1$. In all the calculations, we used the values $m = 55$ and $\alpha = 0.01$.

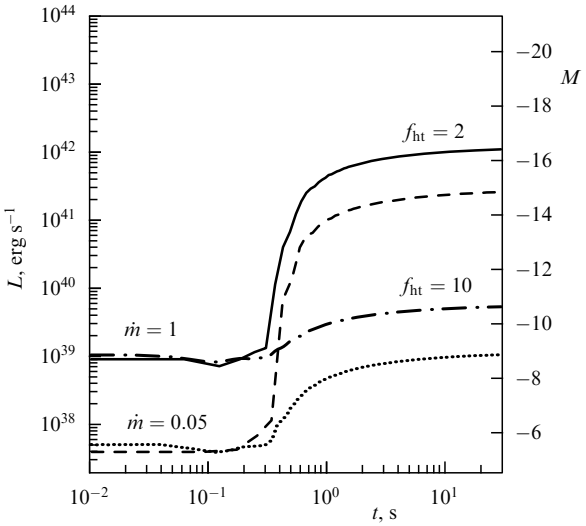

Figure 16. Light curves for four models taking into consideration vertical expansion. Same notations for the curves as in Fig. 15.

5.2 Calculation results

As expected, the main implications of the new model were a drop in gas density behind the SW and a lower temperature increase after shock heating (Figs 13 and 14). The gas density in a convective disk decreased to about four to five times compared with the equilibrium value, while the disk thickness increased by three to five times. In a radiative disk, the density decreased by two to three times. It is noteworthy that taking into account the vertical motion of gas did not lead to a change in the relative contribution of gas pressure.

The peak temperature inside the disk for all models was $(3.0-4.5) \times 10^7$ K (Fig. 15). Due to the difference between heat transport mechanisms, the surface temperature in the models differed more significantly. In convective disks, the temperature reached 2×10^7 K, and the luminosity increased by about 2.5–3 orders of magnitude, to $\gtrsim 2 \times 10^{42}$ erg s^{-1} ($-16.5^{\rm m}$). In radiative disks, the temperature increased to $(3-4.5) \times 10^6$ K, and the luminosity increased by 0.5–1.3 orders of magnitude, to 5×10^{39} erg s^{-1} ($-10.5^{\rm m}$) (Fig. 16).

Figure 17 shows the integrated spectra of electromagnetic radiation for all four models (the convective model with subcritical accretion was only calculated up to 10 s). The maximum of the flux from convective disks falls in the hard X-ray range. If the flux is adjusted to the distance to the source GW170814 [23], 540 Mpc, then the radiation from these disks will be at the limit of sensitivity of the XMM-Newton observatory's EPIC instrument (5σ level, exposure time 10^3 s) [46]. The maximum of the flux from radiative discs lies in the soft X-ray range and, for the parameters of GW170814, is outside the EPIC sensitivity range.

6. Conclusions

The radial structure is determined in sub-Kepler disks primarily by the balance of gravitational and centrifugal forces, while the role of pressure is insignificant. A decrease in the accretor mass violates this balance throughout the disk, but it occurs most strongly in its inner part. The excess of rotation energy is converted into the energy of radial gas motion. A supersonic perturbation wave, which consists of a train of compressions and rarefactions, begins to propagate through the disk. A shock wave emerges within a short time

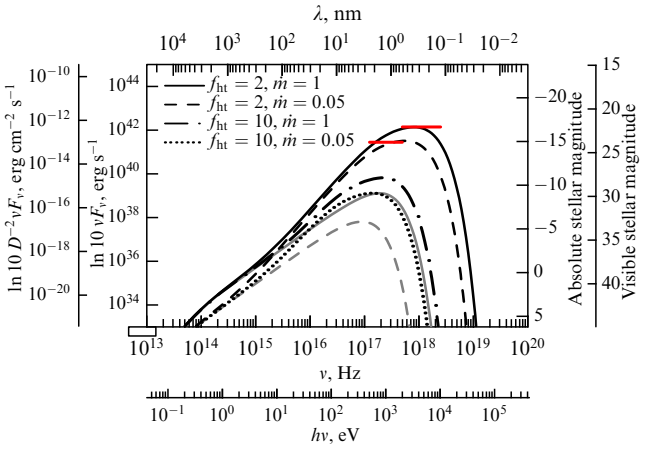

Figure 17. Electromagnetic radiation spectra for models that take into account vertical expansion, in units of luminosity per unit logarithmic frequency interval. Internal vertical scales: luminosity (left) and absolute bolometric stellar magnitude (right). External vertical scales correspond to a source located at a distance of 540 Mpc: flux through a unit detector area (left) and visible stellar magnitude (right). Notations of the black lines are the same as in Fig. 15. The gray curves display spectra of unperturbed disks. Horizontal bars show the lower sensitivity limits of the EPIC-MOS and EPIC-PN detectors of the XMM-Newton observatory (5σ level at an exposure of 10^3 s) [46].

that causes heating of the gas and, as a consequence, brightening of the disk.

We simulated the response of the accretion disk to the loss of 5% of the accretor mass as a result of the merger of a binary BH. The merger parameters correspond to the GW170814 system: an initially binary BH with a total mass of $55\,M_\odot$ located at a distance of 540 Mpc [23]. The calculations were performed for several disk models: the radial structure corresponded to zone B in the α-disk model [27], the vertical thermal structure of the disks corresponded to convective or radiative energy transport mechanisms, and the accretion rate was assumed to be critical or 5% of critical. In the first series of calculations, gas pressure alone was taken into account in the disk. In the second series of calculations, both the gas pressure and the radiation pressure were included in the equation of state of matter. In the third series of calculations, we took into account the possibility of adiabatic cooling (heating) of gas due to its expansion (compression) in the vertical direction.

All three series of models showed qualitatively similar effects: in less than 1 s, the disk luminosity increased to a maximum value of 10^{45} erg s^{-1} in the model with gas pressure and 10^{42} erg s^{-1} in the model that takes into account radiation pressure and vertical expansion. For the given physical model of the accretion disk and accretor parameters, the numerical model contained two free parameters: the temperature difference between the inner layers of the disk and its surface and the accretion rate. Setting this temperature difference, we simulated disks with radiative heat transport or disks with developed convection. The temperature in the inner layers of convective disks proves to be significantly lower than that of radiative disks. The convective disk proves as a result to be more susceptible to shock compression; an increase in the temperature behind the SW is larger in it and, therefore, the luminosity increases more significantly.

Calculations of the thermal radiation spectra have shown that the radiative disk models produce the main flux in the soft X-ray range, while convective models do so in both the soft and hard X-ray ranges. If we take as a model source the object GW170814 located at a distance of 540 Mpc, then a surge of luminosity from the convective disk can be detected by the XMM-Newton observatory's EPIC facility. Observation of this effect in radiative discs requires higher detector sensitivity. With the same sensitivity and the same exposure time (10^3 s), the radiative disk will correspond to the sensitivity region of the soft X-ray-range detector of the EPIC camera if the source is located 3–10 times closer to Earth.

We did not simulate radiation transport in our calculations and, therefore, did not take into account the finite time of emission in calculating the light curve. The characteristic time of radiation diffusion near the inner radius of the disk can be estimated as $t_{\rm rad} \sim \tau_{\rm R} H/c \sim 3-30$ s, where the optical semi-thickness of the disk is $\tau_{\rm R} \sim 10^5 - 10^6$, and its geometric semi-thickness is $H \sim 10^6$ cm. Then, the radiative cooling time will be $t_{\rm cool} \sim t_{\rm rad}(\max T)/T_* \sim 30-300$ s, while in the outer parts of the disk this time is even longer, since it increases with increasing radius (see Eqn (69)). Moreover, the dynamic time (it is also the Keplerian and sonic time) is less than 1 s (see Table 3). Thus, radiative cooling does not affect the light curve shape for several tens or hundreds of seconds.

The authors are grateful to A V Tutukov (Institute of Astronomy, RAS), N I Shakura (Sternberg State Astronomical Institute (GAISh), Moscow State University (MSU)), and K L Malanchev (GAISh MSU) for the discussions. This study was supported by the KP19-270 program.

References

1. Landau L D, Lifshitz E M *The Classical Theory of Fields* (Oxford: Pergamon Press, 1975); Translated from Russian: *Teoriya Polya* (Moscow: Nauka, 1988)
2. Clark J P A, Eardley D M *Astrophys. J.* **215** 311 (1977)
3. Tutukov A V, Yungelson L R *Mon. Not. R. Astron. Soc.* **260** 675 (1993)
4. Lipunov V M, Postnov K A, Prokhorov M E *Astron. Lett.* **23** 492 (1997); *Pis'ma Astron. Zh.* **23** 563 (1997)
5. Abbott B P et al. (LIGO Scientific Collab., Virgo Collab.) *Phys. Rev. X* **9** 031040 (2019)
6. Bogomazov A I, Lipunov V M, Tutukov A V *Astron. Rep.* **51** 308 (2007); *Astron. Zh.* **84** 345 (2007)
7. Tutukov A V, Cherepashchuk A M *Astron. Rep.* **61** 833 (2017); *Astron. Zh.* **94** 821 (2017)
8. Misner C W, Thorne K S, Wheeler J A *Gravitation* (San Francisco: W.H. Freeman, 1973)
9. Peres A *Phys. Rev.* **128** 2471 (1962)
10. Bekenstein J D *Astrophys. J.* **183** 657 (1973)
11. Bode N, Phinney S, in *American Physical Society, APS April Meeting, April 14–17, 2007, Abstracts* (Washington, DC: American Physical Society, 2007) S1.010
12. Megevand M et al. *Phys. Rev. D* **80** 024012 (2009)
13. Kocsis B, Loeb A *Phys. Rev. Lett.* **101** 041101 (2008)
14. Cherepashchuk A M *Phys. Usp.* **59** 910 (2016); *Usp. Fiz. Nauk* **186** 1001 (2016)
15. O'Neill S M et al. *Astrophys. J.* **700** 859 (2009)
16. Corrales L R, Haiman Z, MacFadyen A *Mon. Not. R. Astron. Soc.* **404** 947 (2010)
17. Rosotti G P, Lodato G, Price D J *Mon. Not. R. Astron. Soc.* **425** 1958 (2012)
18. Fitchett M J *Mon. Not. R. Astron. Soc.* **203** 1049 (1983)
19. Pietilä H et al. *Celestial Mech. Dyn. Astron.* **62** 377 (1995)
20. de Mink S E, King A *Astrophys. J. Lett.* **839** L7 (2017)
21. Loeb A *Astrophys. J. Lett.* **819** L21 (2016)
22. Bisikalo D V, Zhilkin A G, Kurbatov E P *Astron. Rep.* **63** 1 (2019); *Astron. Zh.* **96** 3 (2019)

23. Abbott B P et al. (LIGO Scientific Collab., Virgo Collab.) *Phys. Rev. Lett.* **119** 141101 (2017)
24. Artymowicz P, Lubow S H *Astrophys. J.* **421** 651 (1994)
25. Kaigorodov P V et al. *Astron. Rep.* **54** 1078 (2010); *Astron. Zh.* **87** 1170 (2010)
26. Sytov A Yu et al. *Astron. Rep.* **55** 793 (2011); *Astron. Zh.* **88** 862 (2011)
27. Shakura N I, Sunyaev R A *Astron. Astrophys.* **24** 337 (1973)
28. Lipunov V M *Astrophysics of Neutron Stars* (Berlin: Springer-Verlag, 1992)
29. Bardeen J M *Nature* **226** 64 (1970)
30. Thorne K S *Astrophys. J.* **191** 507 (1974)
31. Li L-X, Paczyński B *Astrophys. J.* **534** L197 (2000)
32. Milosavljević M, Phinney E S *Astrophys. J.* **622** L93 (2005)
33. Dong R et al. *Astrophys. J.* **823** 141 (2016)
34. Malanchev K L, Postnov K A, Shakura N I *Mon. Not. R. Astron. Soc.* **464** 410 (2017)
35. Shakura N, Postnov K *Mon. Not. R. Astron. Soc.* **451** 3995 (2015)
36. Lightman A P, Eardley D M *Astrophys. J.* **187** L1 (1974)
37. Velikhov E P *Sov. Phys. JETP* **9** 995 (1959); *Sov. Phys. JETP* **36** 1398 (1959)
38. Chandrasekhar S *Proc. Natl. Acad. Sci. USA* **46** 253 (1960)
39. Balbus S A, Hawley J F *Astrophys. J.* **376** 214 (1991)
40. Sedov L I *Similarity and Dimensional Methods in Mechanics* (Moscow: Mir Publ., 1982); Translated from Russian: *Metody Podobiya i Razmernosti v Mekhanike* 8th ed. (Moscow: Nauka, 1977)
41. Samarskii A A, Popov Yu P *Raznostnye Metody Resheniya Zadach Gazovoi Dinamiki* (Finite Difference Methods for Solving Gas Dynamics Problems) 2nd ed. corr., enl. (Moscow: Nauka, 1980)
42. Samarskii A A, Popov Yu P *Raznostnye Metody Resheniya Zadach Gazovoi Dinamiki* (Finite Difference Methods for Solving Gas Dynamics Problems) 3rd ed. enl. (Moscow: Nauka, 1992)
43. Ginzburg V L *Theoretical Physics and Astrophysics* (Oxford: Pergamon Press, 1979); Translated from Russian: *Teoreticheskaya Fizika i Astrofizika* (Moscow: Nauka, 1975)
44. Illarionov A F, Syunyaev R A *Sov. Astron.* **16** 45 (1972); *Astron. Zh.* **49** 58 (1972)
45. Pavlov G G, Shibanov Yu A, Mészáros P *Phys. Rep.* **182** 187 (1989)
46. Team XMM Newton Community Support. XMM-Newton Users Handbook. Issue 2.16, https://xmm-tools.cosmos.esa.int/external/xmm_user_support/documentation/uhb/XMM_UHB.html (2018)
47. Abbott B P et al. (LIGO Scientific Collab., Virgo Collab.) *Astrophys. J.* **818** L22 (2016)
48. Abbott B P et al. (LIGO Scientific Collab., Virgo Collab.) *Phys. Rev. Lett.* **116** 241103 (2016)
49. Abbott B P et al. (LIGO Scientific Collab., Virgo Collab.) *Phys. Rev. Lett.* **118** 221101 (2017)
50. Abbott B P et al. (LIGO Scientific Collab., Virgo Collab.) *Astrophys. J.* **851** L35 (2017)